A novel approach for modelling microfluidic fuel cell coupling vibration

Tiancheng Ouyang [a,b,*], Feng Zhou [a], Jingxian Chen [a], Jie Lu [a], Nan Chen [b]

[a] College of Mechanical Engineering, Guangxi University, Nanning, PR China
[b] School of Mechanical Engineering, Southeast University, Nanjing, PR China

HIGHLIGHTS

- A mathematical model of microfluidic fuel cell coupling vibration is proposed.
- The effect of vibration intensity, vibration frequency and flow rate is studied.
- Slight vibration reduces the thickness of concentration boundary layer.
- Fuel utilisation decreased by 70% and crossover increased by 80% at high acceleration.

GRAPHICAL ABSTRACT
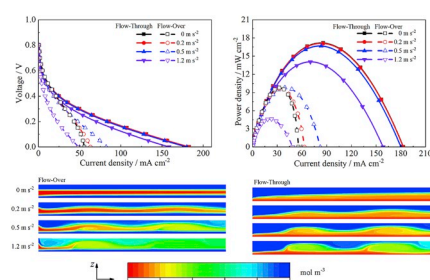
ARTICLE INFO

ABSTRACT

Microfluidic fuel cell (MFC) is an emerging power supply technology for telecommunication base stations and portable instruments that allows long operational time without recharging. Cell performance is severely impaired, however, when the MFC is disturbed by vibrations. To resolve the foregoing problem, a thorough investigation of the vibration mechanism is indispensable. A three-dimensional computational model coupled with multi-physics, including hydrodynamics, electrochemical reaction kinetics, mass transport, and vibration field, is developed for the flow-over and flow-through MFCs in this study. The veracity of the computational model is validated by the agreement between simulation results and experimental data. A comprehensive study, which investigates the influence of vibration parameters (e.g., vibration intensity and frequency) on cell performance, is first conducted to obtain numerical results. The resistance of flow rate and fuel concentration to vibration is thereafter demonstrated. Finally, the effect of vibration on fuel crossover and fuel utilisation is explored. Based on the results of the current study, it is concluded that the anti-vibration property of the flow-through MFC is better than that of the flow-over MFC. The contributions of this study lay the foundation of MFC structure optimisation to further improve the anti-vibration performance.

1. Introduction

With the popularisation and promotion of 5th generation mobile networks (5G) and internet of things, the number of features of devices (i.e., mobile phones, laptops, and in-car computers) continues to increase, correspondingly increasing power consumption [1,2]. There is an urgent demand, therefore, for high-performance batteries with a high power density, diminutive size, and long life [3]. The specific capacity of cathode materials, however, severely limits the energy density, thus posing a threat to the conventional Li-ion battery technology industry

---

* Corresponding author. College of Mechanical Engineering, Guangxi University, Nanning, PR China.
  E-mail address: ouyangtiancheng@gxu.edu.cn (T. Ouyang).

[4]. For economic and social development, it is crucial for researchers and engineers to develop a novel battery technology that can effectively solve the problems of low energy density and short cycle life. Over the past few years, another option, known as fuel cell, has emerged from the electrochemistry domain. These cells exhibit good performance, thus making them a potential replacement of Li-ion batteries because they are pollution-free and have high energy density [5,6].

It is difficult and costly, however, for conventional fuel cells with a proton exchange membrane to be disseminated and extensively applied. Major factors, including the fabrication of graphite bipolar plates, membrane-related problems (ohmic over-potential and management of heat and water), and difficulty in miniaturisation, have to be considered. These problems limit the practical application of various embedded devices and increase the cost for commercial usage [7–9]. Recently, based on the utilisation of laminar flow, a novel membraneless structure of the fuel cell, i.e., the MFC, has resolved the aforementioned problems in the use of conventional fuel cells. The microfluidic fuel cell has been quickly promoted in micro-electro mechanical systems (MEMS) and microfluidic devices mainly because they are diminutive in size, light-weight, convenient to manufacture, and have good heat dissipation capability under high power conditions [10–13].

In order to effect miniaturisation, the membraneless laminar flow-based fuel cell (i.e., MFC) attempts to bridge the gap between the microfluidic device and high power density. As the last century ended, Kenis et al. [14] reported that the phenomenon of multiphase laminar flow inside capillaries lays the foundation for the MFC. After several years, Choban et al. [15] used formic acid as fuel instead of vanadium species. Cohen et al. [16] developed a novel F-shaped microchannel design to improve the MFC performance. Moreover, a T-shaped design was suggested by Bazylak et al. [17] to promote fuel utilisation in the MFC. In the following year, a new inlet is set in the main channel to feed into a third electrolyte stream and separate the oxidant and fuel [18]. By changing the channel aspect ratios and the use of tapered geometry, the MFC performance has considerably improved after solving the crossover problem [19]. Zhang et al. [20] investigated the operating conditions under which the MFC could naturally operate with highly concentrated fuel. Over the years, Tanveer et al. [21,22] have performed a number of investigations on the impact of diverse geometric configurations (e.g., channel, electrodes, inlet locations, and multiple compartments) on membraneless fuel cells. Lee et al. [23] proposed a new planar stack to improve the total power as a high-power source for mobile devices. These designs and fabrications, however, have encountered a difficulty in solving the following problem: only a minimal amount of fuel or oxidant is transported across the electrode surface to active sites, resulting in low fuel utilisation and weakening the MFC performance.

Compared with the MFCs with flow-over anodes and cathodes, MFCs with porous flow-through electrodes have distinct advantages in certain aspects (e.g., mass transfer, geometrically increased effective active area, and practically no restraint on concentration boundary layer) [24–27]. Evidently, its application has not succeeded without numerous experiments. To achieve high performance, Ortiz-Ortega et al. [28] combined flow-through and air-breathing electrodes on the fuel cell. Catalysts and other porous electrode materials have been extensively discussed. In addition, the graphene-carbon nanotube composite aerogel with Ru@Pt nanoparticle, Ni-supported carbon nanotube-coated sponge, and graphene@nickel foam have been considered as porous electrodes that can improve the performance of MFC [29–32]. In recent years, the use of alternative fuels (e.g., ethylene, glycol, and glycerol fuels) instead of traditional fuels has been attempted and yielded beneficial results [33]. Moreover, a new type of bendable MFC can extend its application in powering emerging wearable and flexible electronics [34]. For the physicochemical phenomena in the operation of fuel cells, a numerical model could be developed to optimise the structure and improve performance. Zhang et al. [35] proposed a numerical model for air-breathing microfluidic fuel cells on the foundation of precursors [36]. A comparative study between co-flow and counter-flow MFCs was conducted by Wang et al. [37]. Most numerical studies on ongoing developments of the MFC operate under ideal conditions (e.g., isothermal, negligible body forces, and fully dissolved gas). To further develop and optimise operations, it is crucial to supplement and perfect the application of the MFC under practical operating conditions [38].

Seventeen years after the first MFC was introduced, studies that focused on its performance and structure improvements have been extensively conducted. Reports related to the effect of vibration on MFC performance, however, are limited. In view of the application scenarios of MFC (such as the mobile phone, portable test terminal and wearable devices), anti-vibration is considerably important to fuel cell performance and therefore cannot be ignored. The analysis of vibration in MFC of portable devices is necessary. Hence, it is impractical to optimise performance without including vibration. The core objective of this study is to thoroughly investigate the vibration mechanism and acquire insights on solving problems that are encountered in the daily application of MFCs.

This study focuses on exploring the critical factors of vibration by means of a relatively comprehensive comparison between flow-over and flow-through MFCs under different vibration conditions. The three-dimensional computational models of MFC in a vibrational state are proposed by multi-physics field coupling (e.g., microfluidic hydrodynamics, electrochemical reaction kinetics and species transport of fluid, and vibration field). The reliability of the numerical model is verified by simulation results, which are in good agreement with experimental data. The proposed mathematical model is therefore found reliable in accurately predicting the MFC performance. Furthermore, physical and chemical phenomena and their interactions with the MFC are clearly described in the vibrational state. According to the numerical results, the effect of vibration on cell performance and the inflow rate resistance to vibration are investigated under various conditions, and demonstrated by the polarisation curve, power density curve, fuel concentration distribution, and fuel concentration gradient. Finally, fuel crossover and utilisation are used to describe the vibration resistance of flow-over and flow-through MFCs. Simply put, a set of analytical insights on the effect of vibration on the MFC is proposed to guide future research or provide a reference for performance optimisation in practical scenarios.

2. Geometric configuration

Fig. 1(a) shows the architecture of an air-breathing MFC with a flow-over porous anode. It includes an 18 mm long and 3 mm wide channel, a 0.26 mm thick graphite felt anode (GFA), a 1 mm thick main channel (MC), a 0.02 mm thick cathode catalyst layer (CCL), and a 0.26 mm thick cathode diffusion layer (CDL). The other MFC with a new surplus structure in the GFA, called anode flow channel (AFC), is shown in Fig. 1 (b). The MFC is placed horizontally to ignore gravity effect [39]. Based on the operating principle, the most significant difference between Fig. 1 (a) and (b) is whether the fuel inlet and outlet are at the same channel. In Fig. 1(a), the fuel stream is fed from the surface of anode electrode and then flows in the main channel in parallel with the anode. By contrast, the fluid fuel fills the anode flow channel first, then permeates through the graphite felt anode, and finally flows out of the main channel in Fig. 1(b). The MFC with a flow-through porous anode is found to exhibit a better performance in all aspects, particularly for the full contact with the catalyst layer. Table 1 lists some key parameters and test conditions used in the model.

3. Numerical model

3.1. Modelling assumptions

In establishing the numerical model, there are certain indispensable assumptions on hydromechanics, mass transport, and electrochemical kinetics. The essential assumptions under normal conditions are
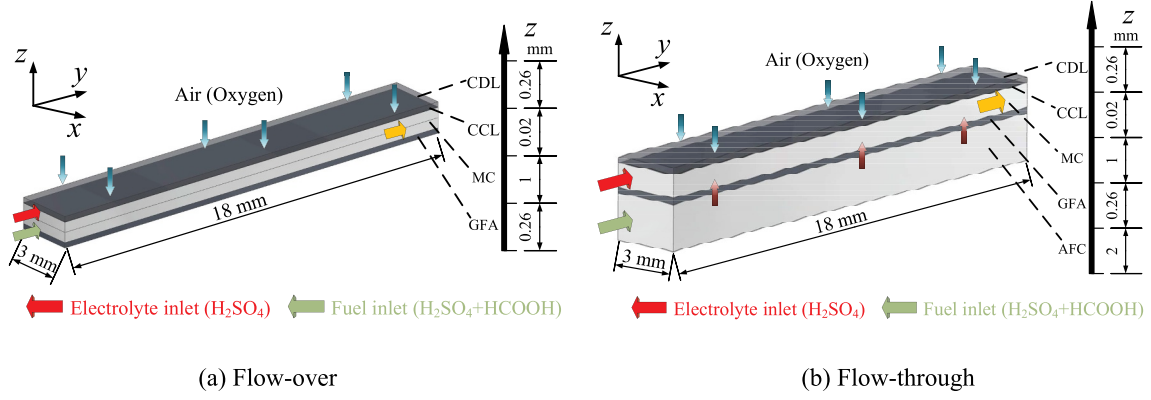
(a) Flow-over

(b) Flow-through

Fig. 1. Schematic illustrations of the air-breathing MFC with flow-over and flow-through porous anodes.

Table 1
Operational parameters of model.

| Parameter	Fluid		Unit
Density, ρ	1000		kg·m^{-3}
Dynamic viscosity, μ	0.001		Pa·s
Conductivity, σ_e	43		S·m^{-1}
Cell temperature, T	298		K
Formic acid inlet concentration, $c_{0,f}$	1000		mol·m^{-3}
Oxygen mass fraction at air and cathode interface, $\omega_{0,O}$	0.228		
Nafion volume fraction within catalyst layers, ε_{Nafion}	0.3		
	Electrode		
	Anode	Cathode	
Diffusion coefficient, D	5×10^{-10}	2.1×1^{-5}	m^2·s^{-1}
Charge transfer coefficient, α	0.5	0.5	
Number of electrons transferred, n	2	4	
Exchange current density, i_0	1.194	1.5×10^{-3}	A·m^{-2}
Reference concentration, $c_{f,ref}$ and $c_{O,ref}$	500	8.5	mol·m^{-3}
	GFA	CDL	CCL
Porosity, $\varepsilon_{fa}, \varepsilon_{dl}, \varepsilon_{cl}$	0.929	0.7	0.4
Permeability, K_{fa}, K_{dl}, K_{cl}	3.45×10^{-12}	1×10^{-12}	1×10^{-15}	m^2
Conductivity, $\sigma_{fa}, \sigma_{dl}, \sigma_{cl}$	1000	1.15×10^4	7.27×10^4	S·m^{-1}

summarised as follows:

(1) isothermal and steady state conditions;
(2) incompressible fluid flow;
(3) gravity neglected but with existing body force;
(4) homogeneous physical properties of electrode and electrolyte;
(5) capacity to carry dilute solutions;
(6) ionic migration and bubble generation neglected;
(7) vibration energy applied to liquids by an artificial body force.

3.2. Governing equations

The MFC model employs formic acid as fuel in the anolyte and applies oxygen as oxidant in the catholyte; both are dissolved into the supporting electrolyte of sulphuric acid.

The electrochemical reaction equation of the formic acid oxidation that occurs on the anode side is given by the following.

$$HCOOH \rightarrow CO_2 + 2H^+ + 2e^-, \quad E^0 = -0.198V \tag{1}$$
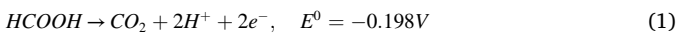
The electrochemical reaction equation of oxygen reduction that

occurs on the cathode side is

$$O_2 + 4H^+ + 4e^- \rightarrow 2H_2O, \quad E^0 = 1.229V \tag{2}$$
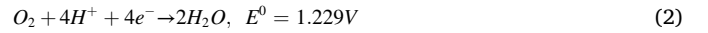
where E and the superscript 0 represent the potential (V) and standard condition, respectively.

3.2.1. Fluid flow

For low Reynolds numbers, the laminar and incompressible flows in the micro-channels can be described by the Navier-Stokes and continuity equations:

$$\nabla \cdot \boldsymbol{u} = 0 \tag{3}$$

$$\rho(\boldsymbol{u} \cdot \nabla)\boldsymbol{u} = -\nabla P + \mu\nabla^2\boldsymbol{u} + \boldsymbol{F} \tag{4}$$

where $\boldsymbol{u}$ is the velocity vector of the channel (m·s^{-1}); ρ is the fluid density of the electrolyte; P is the location pressure (Pa), and $\boldsymbol{F}$ is the body force (N·m^{-3}). Here, Eq. (3) is the mass conservation equation for all calculation regions of the model, and the momentum equation in AFC and MC is described by Eq. (4). The pressure losses in GFA, CCL, and CDL are defined by Brinkman equation. The momentum equations of cellular materials are therefore described by the following:

$$\frac{\rho}{\varepsilon^2} - [(\boldsymbol{u} \cdot \nabla)\boldsymbol{u}] = -\nabla P + \nabla \cdot \left[\frac{1}{\varepsilon}\mu\left(\nabla\boldsymbol{u} + (\nabla\boldsymbol{u})^T - \frac{2}{3}\frac{\mu}{\varepsilon}(\nabla \cdot \boldsymbol{u})I \right) \right] - \frac{\mu}{K}\boldsymbol{u} + \boldsymbol{F} \tag{5}$$

where K is the permeability of the counterpart material; ε is the porosity of the corresponding proportion of material. In Fig. 1(a) and (b), the flow rates of the fuel and electrolyte inlets are equal and constant, and the output pressure of MC is set as 1 bar (equal to the atmospheric pressure). All other wall surfaces are continuous and are in a no-slip boundary state. All parameters used are listed in Table 1.

3.2.2. Charge conservation

In this numerical model, sulphuric acids of the same concentration are used as the supporting electrolyte for both fuel and electrolyte. One of the modelling assumptions that electrical migration becomes the sole proton transport is therefore tenable. The electrical potential in the electrolyte of the channel is defined by

$$\sigma_e\nabla \cdot \nabla\varphi_e = 0 \tag{6}$$

where σ, subscript e, and φ represent the conductivity, solution, and potential, respectively. Similarly, the electrical potential in GFA, CCL, and CDL are given by

$$\sigma_e^{eff}\nabla \cdot \nabla\varphi_e = 0 \tag{7}$$

$$\sigma_s^{eff}\nabla \cdot \nabla\varphi_s = 0 \tag{8}$$

where superscripts *eff* and *s* represent the effective value and electrode, respectively; σ_s^{eff} and σ_e^{eff} are the effective conductivities defined as follows.

$$\sigma_s^{eff} = \left(1 - \varepsilon - \varepsilon_{Nafion}\right)^{1.5}\sigma_s \tag{9}$$

$$\sigma_e^{eff} = \varepsilon^{1.5}\sigma_e \tag{10}$$

The anode profile is set to the ground connection, whereas the cathode head face is set to the cell voltage. The rest of the planes are insulated.

3.2.3. Mass transport

In the flow channel (AFC and MC), the conservation of mass (HCOOH) is defined as follows.

$$\nabla \cdot \left(-D_f^{eff}\nabla c_f + \boldsymbol{u} \cdot \nabla c_f\right) = 0 \tag{11}$$

In porous media (GFA), the conservation of mass (HCOOH) is defined as

$$\nabla \cdot \left(-D_f^{eff}\nabla c_f + \boldsymbol{u} \cdot \nabla c_f\right) = S_f \tag{12}$$

where *D, c, S,* and subscript *f* denote the diffusion coefficient, fuel concentration, reaction source (mol m^{-3}·s^{-1}), and fuel (HCOOH), respectively. The fuel reaction source (S_f) and effective diffusion coefficient (D_f^{eff}) are defined as

$$S_f = -\frac{vi_a}{nF} \tag{13}$$

$$D_f^{eff} = \varepsilon D_f \tag{14}$$

where *v, i_a, n,* and *F* are the mole number, anode current density, number of electron transfer, and Faraday constant (96485 C·mol^{-1}), respectively. At the fuel inlet, the concentration constraint is applied with a fixed concentration, and at the mixture outlet, the convective boundary condition is defined. The rest of the boundaries are in a no-flux state.

For the cathode of the MFC with an air-breathing porous electrode, the oxidant transport process from ambient air (oxygen) could be interpreted as the Maxwell-Stefan principle because the oxygen passes through the cathode (CDL and CCL) only by diffusion action. The Maxwell-Stefan equation is given by

$$\nabla \cdot \left\{-\rho_g \omega \sum_{j=1}^{2} D_O^{eff}\left[\frac{M}{M_j}\left(\nabla\omega_j + \omega_j\frac{\nabla M}{M_j}\right) + (x_j - \omega_j)\frac{\nabla P}{P}\right]\right\} = S_O \tag{15}$$

where ρ_g, *M*, ω, *x*, subscript *j*, and S_O denote the gas density, molecular mass, mass fraction, molar fraction, gas species, and oxygen reaction source, respectively. The density and molecular mass of ambient air are calculated by Eqs. (16) and (17), respectively.

$$\rho_g = M_g\frac{P}{RT} \tag{16}$$

$$M_g = x_{O_2}M_{O_2} + x_{N_2}M_{N_2} \tag{17}$$

The effective diffusivities of gaseous oxygen in CCL and CDL are expressed as follows.

$$D_{O,dl}^{eff} = \varepsilon_{dl}D_O \tag{18}$$

$$D_{O,cl}^{eff} = \varepsilon_{cl}D_O \tag{19}$$

In the CDL, the oxygen diffuses without reaction; therefore, the oxygen reaction source is zero.

$$S_O = 0 \tag{20}$$

In the CCL, the oxygen not only diffuses but also reacts; the oxygen reaction source is therefore not zero.

$$S_O = -\frac{|i_c|}{nF}M_O \tag{21}$$

The top boundary condition of CDL is set as a constant value with respect to the oxygen mass fraction. The rest of the surface is under a zero-flux condition.

3.2.4. Electrochemical reaction kinetics

When an irreversible reaction occurs at the electrode, the electrode potential deviates from the initial equilibrium potential. This phenomenon is called electrode polarisation and categorised as concentration and electrochemical polarisations. The latter is caused by the electrode potential deviation induced by the slow rate of electrochemical process. The relationship between over-potential and current density is controlled by electrochemical polarisation, as described by the Butler-Volmer equation:

$$i_a = Ai_{0,f}\frac{c_f}{c_{f,ref}}\left[e^{\eta\alpha nF/RT} - e^{-\eta(1-\alpha)nF/RT}\right] \tag{22}$$

$$i_c = Ai_{0,O}\frac{c_O}{c_{O,ref}}\left[e^{\eta\alpha nF/RT} - e^{-\eta(1-\alpha)nF/RT}\right] \tag{23}$$

where *A*, η, α, *n* denote the density of catalytic active sites, over-potential, charge transfer coefficient, and number of electron transfer at the limiting step, respectively. Furthermore, η is defined as

$$\eta = \varphi_s - \varphi_e - E_{REV} \tag{24}$$

where φ_e and φ_s are calculated by Eqs. (7) and (8), respectively; E_{REV} is the reversible potential, which is taken as a constant value. Considering the direct effect of device vibration on the MFC, the current loss must be considered as follows.

$$i_{loss} = i_{0,f}\frac{c_f}{c_{f,ref}}e^{\eta\alpha nF/RT} \tag{25}$$

Summarising Eqs. (22)-(25), the total output current of the MFC is calculated by the following.

$$i = i_a - i_c - i_{loss} \tag{26}$$

To compare the effects of current loss on cell performance under different conditions, the loss ratio of the total generated current is defined as follows.

$$\lambda = \frac{i_{loss}}{i + i_{loss}} \times 100\% \tag{27}$$

The maximum fuel utilisation of the MFC is calculated by

$$\xi = \frac{j}{nFc_{0,f}Q} \tag{28}$$

where *j* is the maximum electricity; *n* denotes the electron number of one oxidised formic acid molecule; *Q* is fuel flow.

3.2.5. Excitation vibration

In reality, intense vibrations severely weaken the MFC performance and may even cause a short circuit. To simplify the model, the vibration energy, which is regarded as a superposition of simple harmonic motion, is applied to liquids by an artificial body force, as defined by

$$\begin{cases} F_x = 0 \\ F_y = 0 \\ F_z = \rho \cdot a \cdot [\sin(\pi\nu y) + \sin(2\pi\nu y) + \sin(4\pi\nu y)] \end{cases} \tag{29}$$

where *a* is the acceleration of liquids; ν is the vibration frequency; *y* is the vertical coordinate along the mainstream of the MFC. To provide closer view of liquid vibration, the body forces along the **X**-axis (F_x) and

Y-axis (F_y) are set to zero; however, the body force along the *Z*-axis (F_z) is represented by the superposition of sine waves with different periods.

3.3. Solution procedure

With the foregoing coupled equations and constraint conditions, the swaying MFC model employs COMSOL Multiphysics 5.4 to solve the aforementioned equations using a nonlinear algorithm. An all-hexahedral mesh is used in the numerical model, and a local grid refinement is applied to the electrode based on the flow channel. After multiple grid independence checks, the optimum mesh is selected for 218168 elements to ensure numerical accuracy and computational efficiency. Using the parametric sweep solver (every 0.5 V), current density points and polarisation curves are obtained. The MFC model could be directly solved by a stationary segregated massively parallel multifrontal solver.

4. Model validation

The MFC is mainly composed of anode collector plate, anode permeable electrode, flow field plate, cathode air self-breathing electrode and cathode cover plate. The MFC performance testing [35] used to verify simulation results was conducted in the mode of constant voltage discharge. An electrochemical workstation was used to control the battery voltage from the open state to the short state with a step-size of −100 mV, and the discharge current of the battery was recorded in real time. The discharge time at each voltage was set as 180 s, and the current at the end of discharge was taken as a record under this voltage condition.

The experimental data [35], where 1.0 M HCOOH and 1.0 M H_2SO_4 function as fuels and 1.0 M H_2SO_4 as electrolyte, are used to verify the proposed mathematical model with a flow-through porous anode. Compared with the experimental data, the MFC model has the same parameters (e.g., geometric constructions and boundary conditions). In the MFC model, both entering gas and produced gas are completely dissolved in the solution to eliminate their effect on the flow field and fuel transfer. As shown in Fig. 2(a) and (b), the example simulation results are in good agreement with experimental results. It can therefore be concluded that the proposed mathematical model is reliable in accurately predicting battery performance. In addition, the physical and chemical phenomena and their interactions with the MFC are accurately described.

5. Results and discussions

The operational performance of MFC is considerably affected by vibration, i.e., vibration intensity and vibration frequency. The effects of vibration on the flow-over (F-O) anode and flow-through (F-T) anode

MFCs are discussed in this section. For the flow-over and flow-through MFCs, the numerical results mainly include the effect of vibration on cell performance and the resistance of incoming flow rate to vibration. In order to compare the differences among vibration effects under various conditions, polarisation curve, power density curve, fuel concentration distribution, fuel concentration gradient, fuel crossover, and fuel utilisation are employed to describe the vibration resistance of flow-over and flow-through MFCs. In the following figures, fuel concentration, including GFA, MC and CCL, is distributed.

5.1. Effect of vibration on cell performance

Vibration is generally described by three factors: intensity, frequency, and phase. To simplify the model, the initial phase is set to 0. Vibration acceleration is a key indicator of vibration intensity, and the vibration acceleration defined in this section is in the range 0–1.2 m·s^{-2} under normal conditions. Moreover, the range of vibration frequency is usually less than 100 Hz; hence, 12.89–93.11 Hz is selected by frequency multiplication.

5.1.1. Vibration intensity

Fig. 3 shows the effect of vibration intensity on cell performance at 200 μL·min^{-1}. The vibration frequency is a constant value (12.89 Hz). For the F-O case with 0 m·s^{-2}, the maximum current density is 55.8 mA·cm^{-2}, and the peak power density is 9.8 mW·cm^{-2}. As the F-O vibration intensity increases, the maximum current density and peak power density first increase and thereafter rapidly decrease. For the F-T case with 0 m·s^{-2}, the maximum current density is 183.1 mA·cm^{-2}, and the peak power density is 17.1 mW·cm^{-2}. When the F-T vibration intensity increases, the maximum current density and peak power density gradually decrease and thereafter rapidly decline after exceeding 0.5 m·s^{-2}. Although the F-O and F-T undergo the same change in vibration intensity, the trend variations of maximum current density and peak power density differ.

Fig. 3(c)-3(e) intuitively shows the reasons for the foregoing trend changes (Fig. 3(b)); a 250 mV cell voltage near the maximum power point. With the increase in vibration intensity, the fuel concentration boundary layer of F-O MFC is gradually deteriorates to enhance the cell performance, as shown in Fig. 3(e). The rate of fuel diffusion to the cathode, however, also increases nonlinearly, resulting in further current losses in the cathode. When the vibration intensity exceeds a certain range, the fuel diffusion is practically completely in the second half of the MFC (1.2 m·s^{-2} in Fig. 3(c)). The current loss exceeds the current increase, thus resulting in the degradation of cell performance.

Compared with the change in current density, the change in power density is more considerable and distinct. In the F-T MFC, there is no concentration boundary layer on the anode surface because of its special structure. Hence, vibration does not improve its performance and only
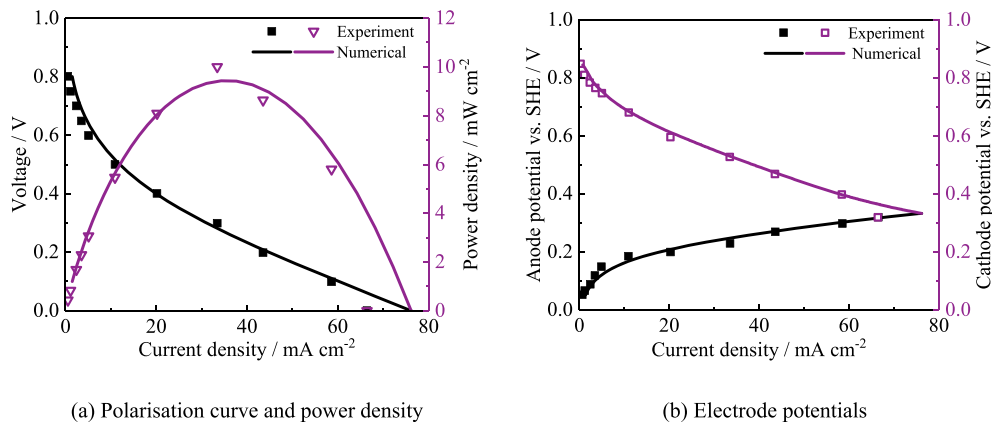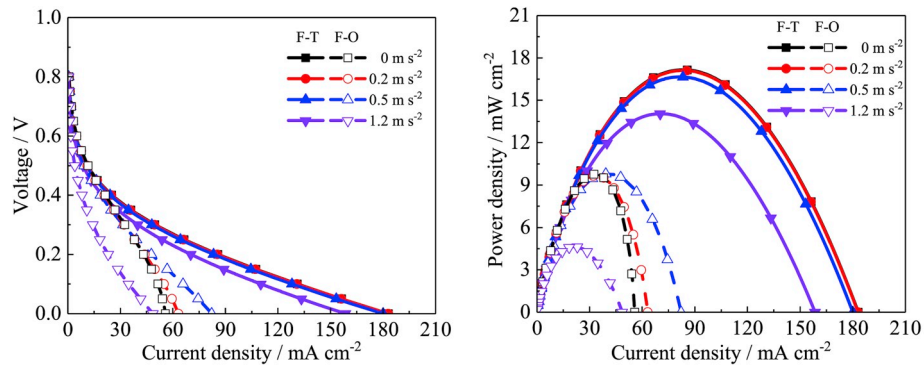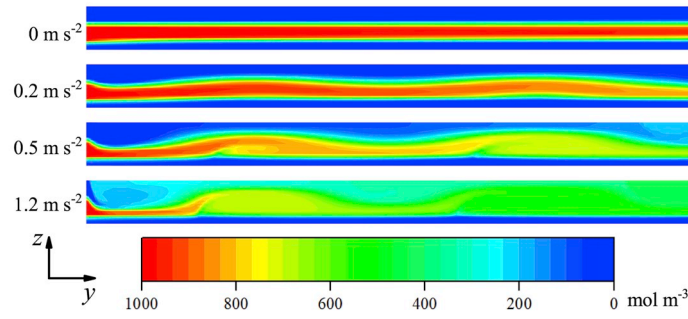

(a) Polarisation curve and power density   (b) Electrode potentials

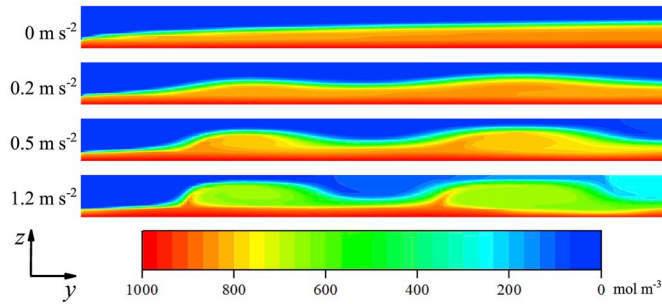**Fig. 2.** Comparison of the numerical results and experimental data.
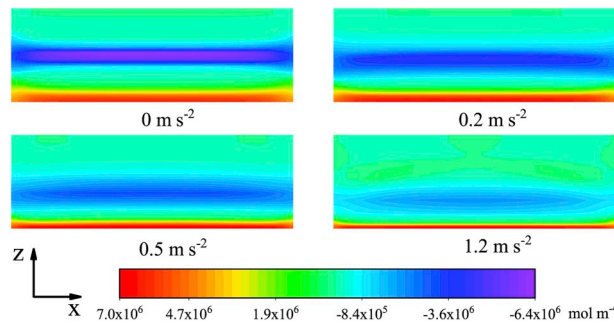
(a) Polarisation curves

(b) Power density curves

(c) Flow-over anode of fuel concentration distribution

(d) Flow-through anode of fuel concentration distribution

(e) Concentration gradient of fuel in X-Z cross section for flow-over anode in main flow channel (Y = 9 mm)

Fig. 3. The effect of vibration intensity on polarisation and power density at the cell voltage of 250 mV.

increases the current loss. Under the same vibration intensity conditions, the rates of fuel diffusion to the cathode of the F-T MFC (Fig. 3(d)) are lower than those of the F-O MFC.

5.1.2. Vibration frequency

Fig. 4 describes the effect of vibration frequency on cell performance under with a 200 μL·min^{-1} flow rate and 0.5 m·s^{-2} acceleration. There is a homogeneous decreasing tendency in current density and power

density with increasing vibration frequency. It is evident that the cell performance of F-O MFC in the vibrational state in terms of power density is worse compared with the F-T MFC. With the increase in vibration frequency from 12.89 to 93.11 Hz, the decrement rates of the maximum current density are 49.97% and 25.40% in the F-O MFC and F-T MFC (Fig. 4(a)), respectively. Similarly, in Fig. 4(b), the loss ratios of the peak power density in the F-T MFC and F-O MFC are equal to 73.01% and 39.26%, respectively. This means that the F-T MFC is approximately twice as effective as the F-O MFC in terms of resisting vibration frequency. Fig. 4(c) and (d) vividly describes the mechanism of fuel concentration distribution that results to such a significant difference.

Fig. 4(c) and (d) shows that a gradual increase in the mixing degree of the fuel and electrolyte is generated along the MC direction in the F-O MFC and F-T MFC as the vibration frequency continues to increase. The specific structure in the F-T MFC, where the fuel channel and electrolyte channel are separated by the GFA layer, leads to a discrepancy in the surface contact between the fuel stream and electrolyte stream ($0 \, \text{m} \cdot \text{s}^{-2}$

in Fig. 3(c) and (d)). Under the same vibration frequency conditions, therefore, the length of the total fuel crossover portion of the F-T MFC (43.50 Hz; Fig. 4(c) and (d)) is shorter than that of the F-O MFC, and the total fuel crossover concentrations are 413 and 379 $\text{mol} \cdot \text{m}^{-3}$ on average, respectively, because of the difference in fuel consumption in the GFA.

5.2. Resistance of flow rate and fuel concentration to vibration

Fig. 5 depicts the cell performance, including the polarisation curve and power density curve, when the vibration frequency and acceleration are set to 12.89 Hz and $0.5 \, \text{m} \cdot \text{s}^{-2}$, respectively.

An evident decreasing trend in current density and power density with a reduced reactant flow rate is found in the aforementioned MFC. Moreover, the declining extent of cell performance in the F-O MFC is worse than that of the F-T MFC. As the flow rate decreases from 400 to 100 $\mu\text{L} \cdot \text{min}^{-1}$, the decrement rates of the maximum current density are
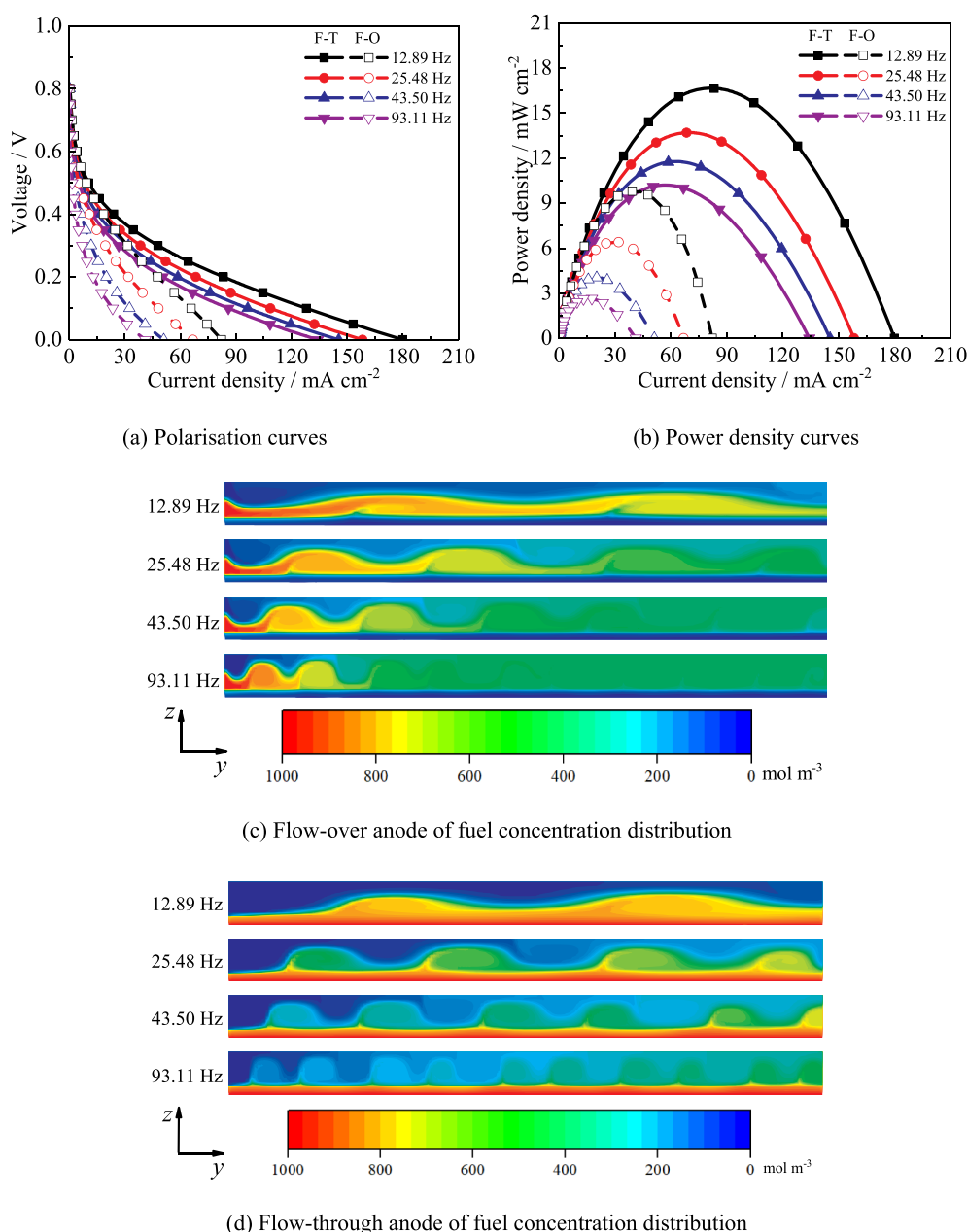

(a) Polarisation curves

(b) Power density curves

(c) Flow-over anode of fuel concentration distribution

(d) Flow-through anode of fuel concentration distribution

Fig. 4. The effect of vibration frequency on polarisation and power density at the cell voltage of 250 mV.

(a) Polarisation curves

(b) Power density curves

(c) Flow-over anode of fuel concentration distribution

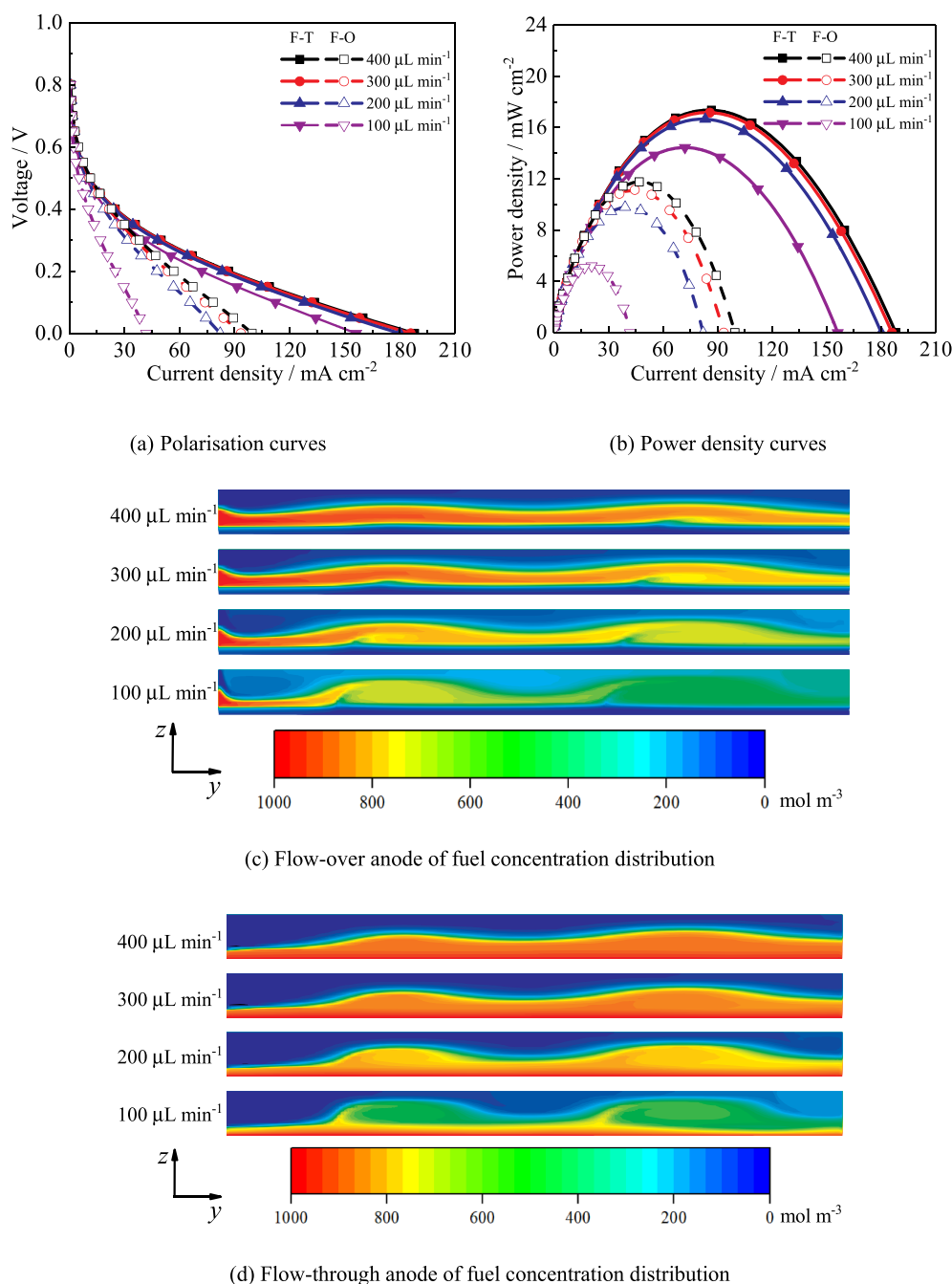(d) Flow-through anode of fuel concentration distribution

Fig. 5. Resistance of flow rate to vibration illustrated by cell performance at the cell voltage of 250 mV.

57.88% and 16.94% in the F-O MFC and F-T MFC, respectively (Fig. 5 (a)), and the attenuation rates of maximum power density are 55.76% and 16.81%, respectively, as shown in Fig. 5(b).

The fuel concentration distributions of F-O MFC and F-T MFC are shown in Fig. 5(c) and (d), respectively. As depicted in Fig. 5(c), a gradual increase in the mixing degree of the fuel and electrolyte is generated along the fuel flow direction in the F-O MFC as the flow rate continues to decrease. Meanwhile, a relatively stable flow condition remains in the F-T MFC, although a slight mixing phenomenon is found in the 100 μL·min^{-1} flow rate, as shown in Fig. 5(d). The fuel crossover of low flow rate indicates that the decreasing flow rate results in a prolonged retention time. The more severe fuel crossover of the F-O MFC results from the fact that the cell structure cannot resist the vibratory action. The specific configuration in which the fuel channel and electrolyte channel are separated by the electrode layer, however, can resist

the vibratory action in the F-T MFC.

The vibration frequency, vibration acceleration, and flow rate are set as 12.89 Hz, 0.5 m·s^{-2}, and 200 μL·min^{-1}, respectively. The polarisation curve and power density curve of the two MFCs with different fuel concentrations are shown in Fig. 6. Fig. 6(a) shows that the current density increment increases first and thereafter decreases with the incremental fuel concentration. Moreover, as the fuel concentration continues to increase, an increasing trend in maximum power density is observed in both F-O MFC and F-T MFC. On the other hand, the peak power density increment increases initially and thereafter decreases (Fig. 6(b)). This is because the reactant transport firstly intensifies, and hydraulic instability is thereafter generated when the fuel concentration increases continuously.

Fig. 6 shows the fuel concentration distributions of F-O MFC and F-T MFC. The stabilised flow condition is held in the F-O MFC, as shown in
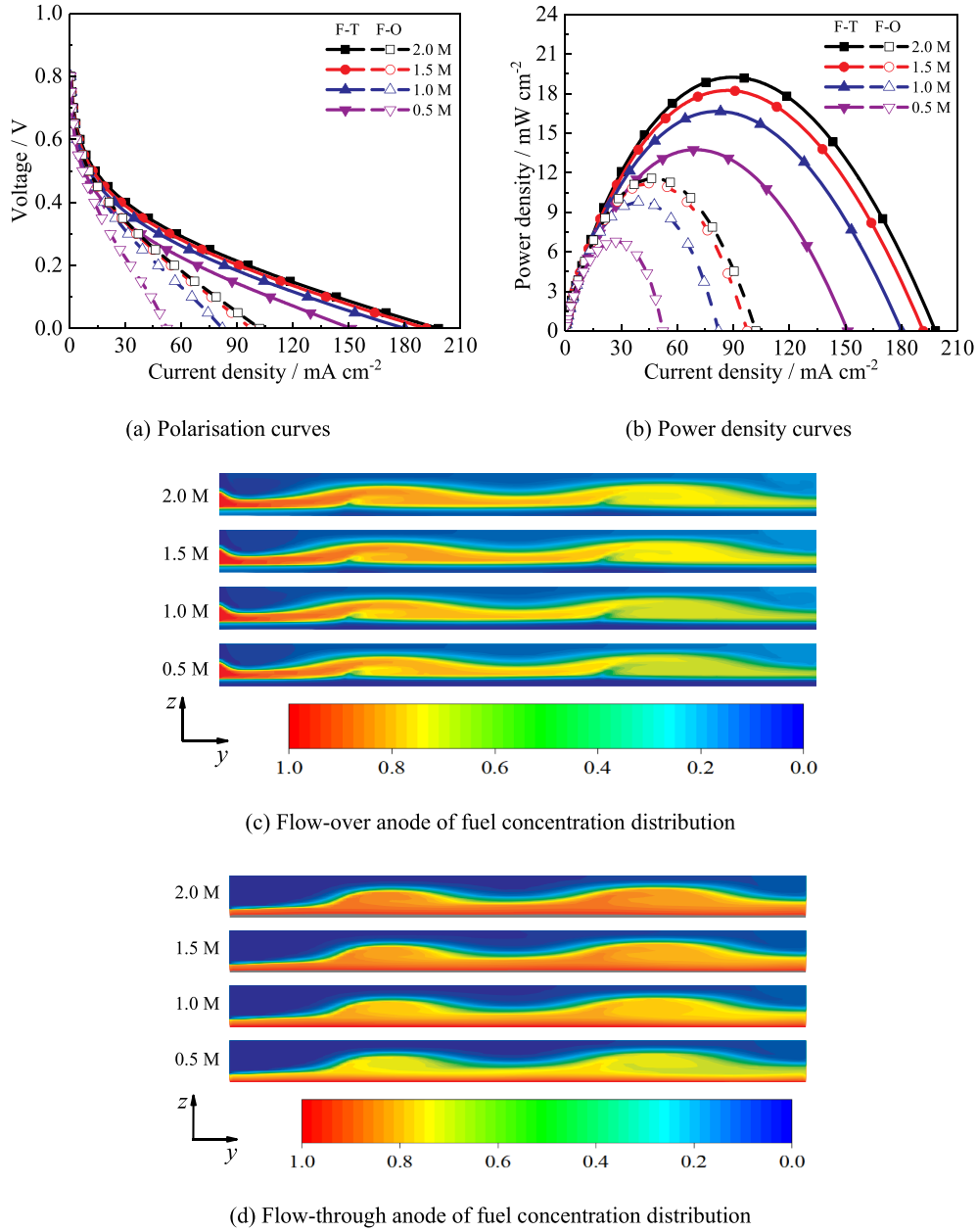
(a) Polarisation curves

(b) Power density curves

(c) Flow-over anode of fuel concentration distribution

(d) Flow-through anode of fuel concentration distribution

Fig. 6. Resistance of fuel concentration to vibration illustrated by cell performance at the cell voltage of 250 mV.

Fig. 6(c). The fuel flow state of the F-T MFC is similar to that of the F-O MFC (Fig. 6(d)). Regardless of whether the fuel concentration increases or not, a severe mixing zone is not generated in the channel. This indicates that the fuel concentration has minimal or no resistance to vibration.

5.3. Effect of vibration on fuel crossover

The effects of vibration on fuel crossover are compared using the loss ratio of the total generated current between F-O MFC and F-T MFC. The loss ratio of F-T MFC is generally less than that of the F-O MFC, regardless of the conditions. Furthermore, the following detailed discussions on the effective factors of vibration reveal different characteristics that can thereby promote a deeper understanding of the effect of vibration on cell performance.

Fig. 7(a) shows a curve-like parabola, which slowly increases initially and then rapidly increases in the loss ratio with increasing F-O MFC vibration intensity. On the other hand, the curve pertaining to the

F-T MFC is characterised by relatively smooth changes. On the contrary, as the vibration frequency increases, the curve of the loss ratio (e.g., logarithmic curve) exhibits the variation trend (Fig. 7(b)).

The loss ratios of F-O MFC and F-T MFC shown in Fig. 7(c) indicate that provided the flow rate is sufficiently large, the effect of vibration can be completely eliminated. In considering Figs. 5 and 8, however, it is noted that the foregoing has to be at the expense of fuel utilisation, and power increase is not significant. Because the concentration varies in a small range, so the diffusion coefficient is assumed to be constant [20]. As a result of the constant diffusion coefficient (Fig. 7(d)), the loss ratio is also constant, which is consistent with the concentration distribution shown in Fig. 6. This indicates that fuel concentration has minimal or no resistance to vibration.

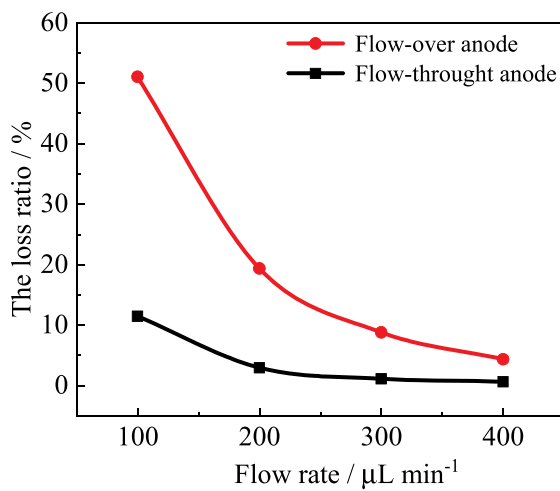### 5.4. Effect of vibration on fuel utilisation

Fig. 8 compares the effect of vibration on fuel utilisation at different flow rates between F-O MFC and F-T MFC. As depicted in Fig. 8(a), an
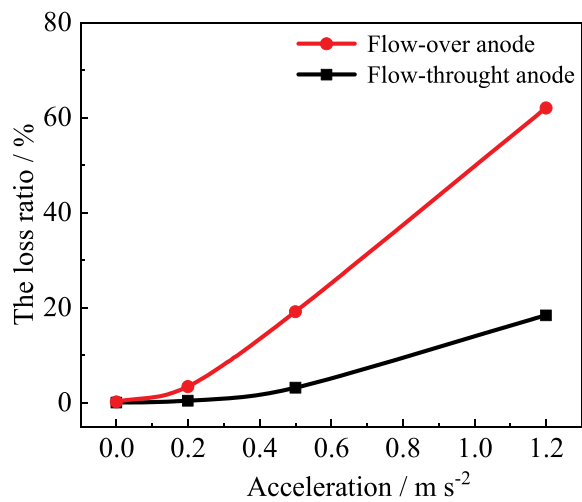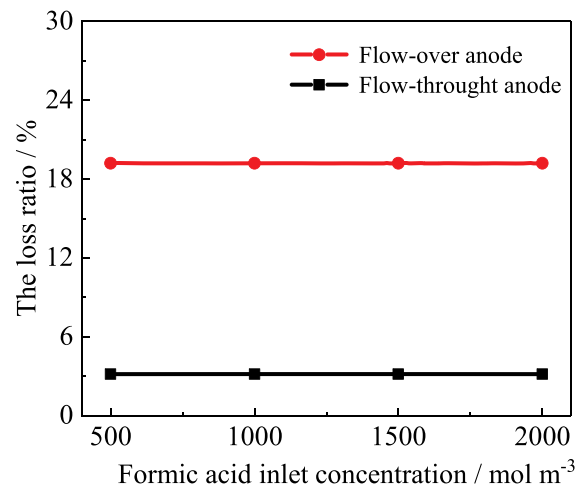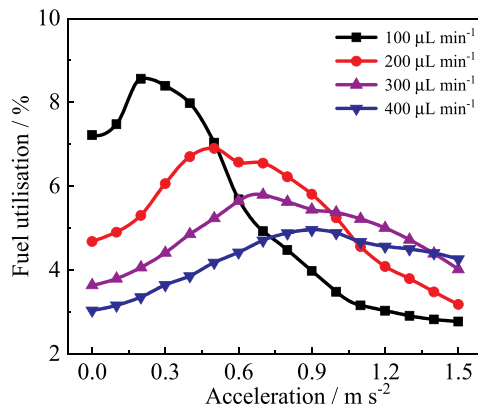
(a) Vibration intensity
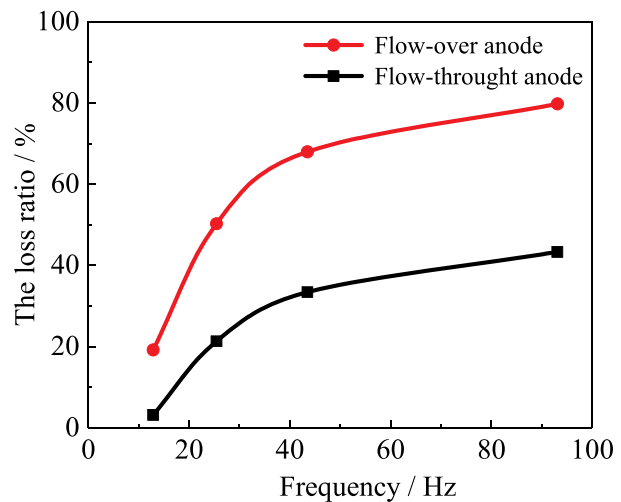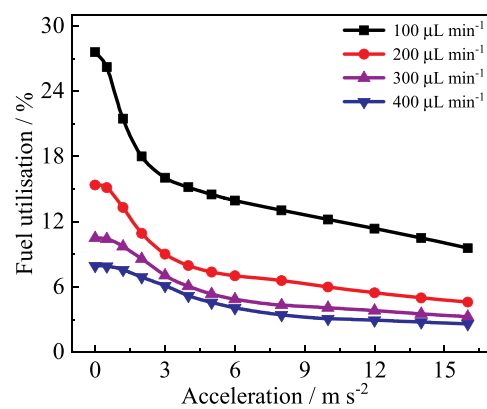
(b) Vibration frequency

(c) Flow rate

(d) Fuel concentration

Fig. 7. The effect of vibration on the loss ratio of the total generated current.

(a) Flow-over anode

(b) Flow-through anode

Fig. 8. The effect of vibration on fuel utilisation.

apparent tendency in which fuel utilisation first increases and thereafter decreases with increasing flow rate under vibration action is found in the F-O MFC. It is evident that the peak value of fuel utilisation shifts rightward and downward as the flow rate continuously increases. This is because of the fact that with the flow rate increasing, the proportion of unreacted fuel to total fuel also goes up significantly, that is to say the peak value of fuel utilisation decreases.

In addition, fuel utilisation tends to decrease when the acceleration is larger than the corresponding value at the maximum fuel utilisation, as shown in Fig. 8(a). Fuel utilisation sharply decreases when the flow rate is $100\,\mu L \cdot min^{-1}$, and the declining tendency is limited by the increasing flow rate. When the flow rate reaches $400\,\mu L \cdot min^{-1}$, a slight downtrend is found under vibration action. This suggests that the effect of vibration is resisted by the increasing flow rate, but the fuel utilisation is compromised.

Fig. 8(b) shows that vibration action can cause the decrease in fuel utilisation, and the slope of the descending curve turns toward diminution with the increasing flow rate. When the flow rate increases from 100 to $400\,\mu L \cdot min^{-1}$ with an interval of $100\,\mu L \cdot min^{-1}$ under the vibration action, the peak fuel utilisation values of the F-O MFC are 8.56%, 6.90%, 5.79%, and 4.96%, whereas the corresponding peak values in the F-T MFC are 27.59%, 15.37%, 10.47%, and 7.93%, respectively. The relatively considerable fuel utilisation of the F-T is because of the unique cell configuration, which is capable of resisting vibration action.

In Fig. 8, the acceleration initially increases from $0\,m \cdot s^{-2}$, but when the acceleration of the F-O MFC is $1.5\,m \cdot s^{-2}$, its fuel utilisation remains stable and nearly constant. The acceleration can reach up to $16\,m \cdot s^{-2}$ in the F-T MFC. The calculation ranges of the two are therefore different. It is found that the F-T MFC is superior to the F-O MFC in terms of vibration resistance.

6. Conclusions

In this study, the critical factors of vibration on the performance of the flow-over MFC and flow-through MFC are discussed in detail. Three-dimensional computational models of the MFC are solved by multiphysics field coupling in the vibrational state. Through individual and comprehensive analyses of multifactorial results, remarkable conclusions are drawn.

(1) Vibration generally weakens the MFC performance; in some cases, however, a slight vibration can enhance fuel transfer.
(2) As the vibration intensity increases, the fuel concentration boundary layer on the surface of flow-over MFC gradually deteriorates and enhances cell performance.
(3) In terms of vibration resistance, the flow-through MFC is superior to the flow-over MFC.
(4) Current density and power density have a distinct decreasing trend with the reduced flow rate of the reactant.
(5) When the fuel concentration increases, the severe mixing zone does not exhibit a significant change in channel, indicating that fuel concentration has no effect on vibration.
(6) Regardless of vibration conditions, the loss ratio of flow-through MFC is less than that of flow-over MFC.
(7) From 100 to $400\,\mu L \cdot min^{-1}$, the fuel utilisation of the flow-over MFC first increases and thereafter decreases with the increase in vibration intensity; however, that of the flow-through MFC continuously decreases.

Declaration of competing interest

None.

References

[1] M. Yan, C.A. Chan, A.F. Gygax, J. Yan, L. Campbell, A. Nirmalathas, C. Leckie, Modeling the total energy consumption of mobile network services and applications, Energies 12 (2019) 1–18.

[2] R. Alhumaima, Evaluation of Power Consumption and Trade-Offs in 5G Mobile Communications Networks, Brunel University London, 2017.

[3] X. Luo, J. Wang, M. Dooner, J. Clarke, Overview of current development in electrical energy storage technologies and the application potential in power system operation, Appl. Energy 137 (2015) 511–536.

[4] N. Nitta, F. Wu, J.T. Lee, G. Yushin, Li-ion battery materials: present and future, Mater. Today 18 (2015) 252–264.

[5] C.K. Dyer, Fuel cells for portable applications, J. Power Sources 106 (2002) 31–34.

[6] J. Xuan, M.K H Leung, D.Y. C Leung, M. Ni, H.Z. Wang, Hydrodynamic focusing in microfluidic membraneless fuel cells: breaking the trade-off between fuel utilization and current density, Int. J. Hydrogen Energy 36 (2011) 11075–11084.

[7] L.Y. Ma, W.W. Cai, J. Li, K. Fan, Y. Jiang, L. Ma, H.S. Chen, A high performance polyamide-based proton exchange membrane fabricated via construction of hierarchical proton conductive channels, J. Power Sources 302 (2016) 189–194.

[8] A. Ghanbarian, M.J. Kermani, Enhancement of PEM fuel cell performance by flow channel indentation, Energy Convers. Manag. 110 (2016) 356–366.

[9] J.P. Meyers, H.L. Maynard, Design considerations for miniaturized PEM fuel cells, J. Power Sources 109 (2002) 76–88.

[10] R. Ferrigno, A.D. Stroock, T.D. Clark, M. Mayer, G.M. Whitesides, Membraneless vanadium redox fuel cell using laminar flow, J. Am. Chem. Soc. 124 (2002) 12930–12931.

[11] M.M. Sabry, A. Sridhar, D. Atienza, P. Ruch, B. Michel, Integrated microfluidic power generation and cooling for bright silicon MPSoCs, IEEE (2014) 1–6.

[12] J. Xuan, M.K.H. Leung, D.Y. C Leung, H.Z. Wang, Laminar flow-based fuel cell working under critical conditions: the effect of parasitic current, Appl. Energy 90 (2012) 87–93.

[13] M.S. Shamim, R.S. Narde, J.L. Gonzalez-Hernandez, A. Ganguly, J. Venkatarman, S.G. Kandlikar, Evaluation of wireless network-on-chip architectures with microchannel-based cooling in 3D multicore chips, Sustain. Comput. Informatics Syst. 21 (2019) 165–178.

[14] P.J.A. Kenis, R.F. Ismagilov, G.M. Whitesides, Microfabrication inside capillaries using multiphase laminar flow patterning, Science 285 (1999) 83–85.

[15] E.R. Choban, L.J. Markoski, A. Wieckowski, P.J.A. Kenis, Microfluidic fuel cell based on laminar flow, J. Power Sources 128 (2004) 54–60.

[16] J.L. Cohen, D.A. Westly, A. Pechenik, H.D. Abruña, Fabrication and preliminary testing of a planar membraneless microchannel fuel cell, J. Power Sources 139 (2005) 96–105.

[17] A. Bazylak, D. Sinton, N. Djilali, Improved fuel utilization in microfluidic fuel cells: a computational study, J. Power Sources 143 (2005) 57–66.

[18] M.H. Sun, G. Velve Casquillas, S.S. Guo, J. Shi, H. Ji, Q. Ouyang, Y. Chen, Characterization of microfluidic fuel cell based on multiple laminar flow, Microelectron. Eng. 84 (2007) 1182–1185.

[19] A. Ebrahimi Khabbazi, A.J. Richards, M. Hoorfar, Numerical study of the effect of the channel and electrode geometry on the performance of microfluidic fuel cells, J. Power Sources 195 (2010) 8141–8151.

[20] H. Zhang, J. Xuan, H. Xu, M.K.H. Leung, D.Y.C. Leung, L. Zhang, H. Wang, L. Wang, Enabling high-concentrated fuel operation of fuel cells with microfluidic principles: a feasibility study, Appl. Energy 112 (2013) 1131–1137.

[21] M. Tanveer, K.Y. Kim, Effects of geometric configuration of the channel and electrodes on the performance of a membraneless micro-fuel cell, Energy Convers. Manag. 136 (2017) 372–381.

[22] M. Tanveer, K.Y. Kim, Performance analysis of microfluidic fuel cells with various inlet locations and multiple compartments, Energy Convers. Manag. 166 (2018) 328–336.

[23] S.H. Lee, Y. Ahn, A laminar flow-based single stack of flow-over planar microfluidic fuel cells, J. Power Sources 351 (2017) 67–73.

[24] L. Li, S. Bei, Q. Xu, K. Zheng, Y. Zheng, Role of electrical resistance and geometry of porous electrodes in the performance of microfluidic fuel cells, Int. J. Energy Res. 42 (2018) 1277–1286.

[25] Y.D. Herlambang, J.C. Shyu, S.C. Lee, Numerical simulation of the performance of air-breathing direct formic acid microfluidic fuel cells, Micro & Nano Lett. 12 (2017) 860–865.

[26] Y. Wang, D.Y.C. Leung, H. Zhang, J. Xuan, H. Wang, Numerical investigation and optimization of vapor-feed microfluidic fuel cells with high fuel utilization, Electrochim. Acta 261 (2018) 127–136.

[27] O.B. Rizvandi, S. Yesilyurt, Modeling and performance analysis of branched microfluidic fuel cells with high utilization, Electrochim. Acta 318 (2019) 169–180.

[28] E. Ortiz-Ortega, M.A. Goulet, J.W. Lee, M. Guerra-Balcázar, N. Arjona, E. Kjeang, J. Ledesma-García, L.G. Arriaga, A nanofluidic direct formic acid fuel cell with a combined flow-through and air-breathing electrode for high performance, Lab Chip 14 (2014) 4596–4598.

[29] D. Li, H. Xu, L. Zhang, D.Y.C. Leung, F. Vilela, H. Wang, J. Xuan, Boosting the performance of formic acid microfluidic fuel cell: oxygen annealing enhanced Pd@ graphene electrocatalyst, Int. J. Hydrogen Energy 41 (2016) 10249–10254.

[30] H. Zhang, Y. Wang, Z. Wu, D.Y.C. Leung, A direct urea microfluidic fuel cell with flow-through ni-supported-carbon-nanotube-coated sponge as porous electrode, J. Power Sources 363 (2017) 61–69.

[31] Y.H. Kwok, Y.F. Wang, A.C.H. Tsang, D.Y.C. Leung, Graphene-carbon nanotube composite aerogel with Ru@ Pt nanoparticle as a porous electrode for direct methanol microfluidic fuel cell, Appl. Energy 217 (2018) 258–265.

[32] Y. Yang, D. Ye, X. Zhu, Q. Liao, J. Li, R. Chen, Boosting power density of microfluidic biofuel cell with porous three-dimensional graphene@ nickel foam as flow-through anode, Int. J. Hydrogen Energy 43 (2018) 18516–18520.

[33] C.A. Martins, O.A. Ibrahim, P. Pei, E. Kjeang, Towards a fuel-flexible direct alcohol microfluidic fuel cell with flow-through porous electrodes: assessment of methanol, ethylene glycol and glycerol fuel, Electrochim. Acta 271 (2018) 537–543.

[34] Y. Yang, Y. Xue, H. Zhang, H. Chang, Flexible H2O2 microfluidic fuel cell using graphene/Prussian blue catalyst for high performance, Chem. Eng. J. 369 (2019) 813–817.

[35] B. Zhang, D.D. Ye, P.C. Sui, N. Djilali, X. Zhu, Computational modeling of air-breathing microfluidic fuel cells with flow-over and flow-through anodes, J. Power Sources 259 (2014) 15–24.

[36] J. Xuan, D.Y.C. Leung, H. Wang, M.K.H. Leung, B. Wang, M. Ni, Air-breathing membraneless laminar flow-based fuel cells: do they breathe enough oxygen? Appl. Energy 104 (2013) 400–407.

[37] Y. Wang, D.Y.C. Leung, H. Zhang, J. Xuan, H. Wang, Numerical and experimental comparative study of microfluidic fuel cells with different flow configurations: Co-flow vs. counter-flow cell, Appl. Energy 203 (2017) 535–548.

[38] H. Wang, X. Zhu, B. Zhang, D. Ye, R. Chen, Q. Liao, Two-phase computational modelling of a membraneless microfluidic fuel cell with a flow-through porous anode, J. Power Sources 420 (2019) 88–98.

[39] J. Xuan, M.K.H. Leung, D.Y. C Leung, H.Z. Wang, Towards orientation-independent performance of membraneless microfluidic fuel cell: understanding the gravity effects, Appl. Energy 90 (2012) 80–86.

NomenclatureSymbol

a: the acceleration of the liquids (m s^{-2})
A: Volume specific surface area (m^2/m^3)
C: concentration (mol m^{-3})
D: diffusion coefficient (m^2 s^{-1})

E: voltage (V)
i$_0$: exchange current density (A m^{-2})
j: maximum output current (A)
K: permeability (m^2)
n: number of electrons transferred
Q: fuel flow rate (μL min^{-1})
R: gas constant (J mol^{-1} K^{-1})
S: reaction source (mol m^{-3} s^{-1})
v: the vibration frequency (Hz)
w$_0$: mass fraction
α: charge transfer coefficient
β: reaction order
ε: porosity
η: activation overpotential (V)
λ: the loss ratio (%)
μ: dynamic viscosity (Pa s)
ξ: fuel utilisation (%)
ρ: density (kg m^{-3})
σ: conductivity (S m^{-1})
τ: tortuosity
Subscripts
a: anode
c: cathode
cl: cathode catalytic layer
dl: cathode diffusion layer
e: electrolyte
f: fuel
fa: graphite felt anode
j: gas species
loss: loss current
O: oxygen
ref: reference value
REV: reversible
s: electrode
Superscript
0: standard value
eff: effective value